

Activation pathway of a G protein-coupled receptor uncovers conformational intermediates as novel targets for allosteric drug design

Xinheng He

Key Laboratory of Cell Differentiation and Apoptosis of Chinese Ministry of Education, Shanghai Jiao Tong University, School of Medicine, Shanghai 200025, China <https://orcid.org/0000-0001-7813-5480>

Zhao Yang

Key Laboratory Experimental Teratology of the Ministry of Education and Department of Physiology, Shandong University School of Medicine, 44 Wenhua Xi Road, Jinan, Shandong, 250012

Zong-Tao Chai

Second Military Medical University

Junyan Wang

School of Medicine, Shandong University

Ashfaq Rehman

Shanghai Jiao Tong University School of Medicine

Duan Ni

State Key Laboratory of Oncogenes and Related Genes, Renji Hospital, Shanghai Jiao Tong University School of Medicine, Shanghai 200127 <https://orcid.org/0000-0002-3902-2843>

Jun Pu

Ren ji Hospital, School of Medicine, Shanghai Jiao Tong University

Jinpeng Sun

Key Laboratory Experimental Teratology of the Ministry of Education and Department of Biochemistry and Molecular Biology, Shandong University School of Medicine

Jian Zhang

Shanghai Jiao Tong University School of Medicine <https://orcid.org/0000-0002-6558-791X>

Shaoyong Lu (✉ lushaoyong@yeah.net)

Shanghai Jiaotong University School of Medicine

Article

Keywords: G protein-coupled receptors, Molecular dynamics simulations, Markov state model, Allosteric mechanisms, Cryptic binding site

Posted Date: November 16th, 2020

DOI: <https://doi.org/10.21203/rs.3.rs-104911/v1>

License:  This work is licensed under a Creative Commons Attribution 4.0 International License.

[Read Full License](#)

Version of Record: A version of this preprint was published at Nature Communications on August 5th, 2021. See the published version at <https://doi.org/10.1038/s41467-021-25020-9>.

Activation pathway of a G protein-coupled receptor uncovers conformational intermediates as novel targets for allosteric drug design

Xinheng He^{1,§}, Zhao Yang^{2,§}, Zong-Tao Chai^{3,§}, Junyan Wang², Ashfaq Ur Rehman¹, Duan Ni⁴, Jun Pu⁵, Jinpeng Sun^{2,✉}, Jian Zhang^{1,6✉}, and Shaoyong Lu^{1,✉}

¹Department of Pathophysiology, Key Laboratory of Cell Differentiation and Apoptosis of Chinese Ministry of Education, Shanghai Jiao Tong University, School of Medicine, Shanghai 200025, China

²Department of Biochemistry and Molecular Biology, Key Laboratory Experimental Teratology of Chinese Ministry of Education, School of Medicine, Shandong University, Jinan, Shandong 250012, China

³Department of Hepatic Surgery VI, Eastern Hepatobiliary Surgery Hospital, Second Military Medical University, Shanghai 200438, China.

⁴The Charles Perkins Centre, University of Sydney, Sydney, NSW 2006, Australia

⁵Department of Cardiology, Renji Hospital, Shanghai Jiao Tong University, School of Medicine, Shanghai 200120, China

⁶School of Pharmaceutical Sciences, Zhengzhou University, Zhengzhou 450001, China

[§]These authors contributed equally to this work.

✉To whom correspondence should be addressed:

Dr. Shaoyong Lu; E-mail: lushaoyong@yeah.net

Dr. Jian Zhang; E-mail: jian.zhang@sjtu.edu.cn

Dr. Jinpeng Sun; E-mail: sunjinpeng@sdu.edu.cn

Abstract

G protein-coupled receptors (GPCRs) are the most frequent targets of approved drugs. A complete mechanistic elucidation of large-scale conformational transitions underlying the activation mechanisms of GPCRs is of critical importance for therapeutic drug development. Here, we utilized a combined computational and experimental framework that integrated extensive molecular dynamics simulations, Markov state models, and site-directed mutagenesis for investigating the conformational landscape of activation of the angiotensin II (AngII) type 1 receptor (AT1R), a prototypical class A GPCR. Our findings suggested a synergistic transition mechanism of AT1R activation. Importantly, a key intermediate state was found in the activation pathway. We discovered a novel “cryptic” binding site in the intracellular region of the receptor in the intermediate state. Furthermore, a bioluminescence resonance energy transfer analysis revealed the insensitivity of the endogenous AngII octapeptide agonist in the activation of the downstream Gq signaling and β -arrestin-mediated pathways, upon mutations of the predicted cryptic binding site, thereby suggesting an allosteric regulatory mechanism. Together, these findings not only provide a deeper understanding of AT1R activation at an atomic level, but also open potential avenues for the design of allosteric AT1R modulators. Consequently, this will provide a broad range of applications for GPCR biology, biophysics, and medicinal chemistry.

Keywords: G protein-coupled receptors; Molecular dynamics simulations; Markov state model; Allosteric mechanisms; Cryptic binding site

As the largest superfamily of cell surface proteins in the human genome, G protein-coupled receptors (GPCRs) represent the therapeutic targets of nearly one-third of all approved drugs^{1,2}. These receptors share a conserved structural architecture of seven transmembrane (7TM) helices linked by three extra- (ECLs) and three intra-cellular loops (ICLs)³. The GPCR-mediated signal transduction is triggered by an extracellular signal to the orthosteric site located in the extracellular region, which then transduces the stimuli to the intracellular region, thereby leading to the engagement of the receptor with G proteins or β -arrestins⁴⁻⁶. The orthosteric site within the 7TM helices is highly conserved across the members of a single GPCR subfamily, and thus poses a significant challenge in the development of selective drugs that can bind to a unique receptor subtype. As an alternative strategy, targeting a binding site outside the conserved orthosteric site, also termed as an “allosteric site,” may provide new avenues for the design of modulators with desirable selectivity profiles⁷⁻¹², which is a long-standing bottleneck in GPCR drug discovery.

Recent technological breakthroughs in receptor engineering have led to a significant increase in the number of available GPCR structures determined by X-ray crystallography and cryo-electron microscopy (cryo-EM)¹³. The solved structures of GPCRs, either in the inactive, antagonist-bound or active, agonist-bound conformations, not only provide mechanistic insights into the agonist-dependent receptor activation mechanisms, but are also useful for investigating structure-based drug design^{14,15}. However, these high-resolution structures represent static snapshots taken under specific experimental conditions, and hence may miss information of the conformational ensemble of the receptors because the receptors may have undergone a large-scale conformational transition during their (de)activation process^{16,17}. Therefore, mechanistic and structural elucidation of the (de)activation pathway of the GPCRs is of paramount importance as distinct conformational states, such as intermediate, metastable, or transient states, present during the inactive-to-active transitions (or vice versa) of the receptors, are desired for a rational design of selective modulators.

The angiotensin II (AngII) type 1 receptor (AT1R), a prototypical class A GPCR, offers an important model for mechanistic exploration as it is a prominent therapeutic target for hypertension and related cardiovascular diseases¹⁸, and also because of the recent

availability of its high-resolution structures in both inactive, antagonist-bound¹⁹ and active, agonist-bound conformations^{20–22}. On comparing the structures of its inactive, antagonist-bound state (ZD7155; PDB ID: 4YAY)¹⁹ (Fig. 1A) and the active state i.e., AT1R complexed with a partial agonist S118 peptide and a G-protein mimetic nanobody (PDB ID: 6DO1)²⁰ (Fig. 1B), the most remarkable differences in the two structures are found in the TMs 5–7 and helix 8 (Fig. 1C). Notably, on the intracellular side, the active state structure exhibits an outward displacement of TM5 and TM6, inward movement of TM7, and substantial repositioning of helix 8 parallel to the membrane, relative to the inactive state structure (Fig. 1C). On the extracellular side, the major conformational changes include an inward shift of TM5 and TM7 in the active state structure compared with the changes in the inactive state structure. Although the static, active, and inactive states of AT1R exhibit marked structural divergences, it has been challenging to completely capture the large-scale conformational transitions along the activation pathway of AT1R by experiments. As such, it remains unclear how a dynamic pathway connects the inactive-to-active conformational transitions, and thereby hinders the deeper understanding of the comprehensive landscape of the underlying activation mechanism of this receptor. Furthermore, there are no allosteric modulators of AT1R reported to date; this suggests a lack of potential allosteric binding sites in the active and inactive state structures of the receptor. Thus, it is advisable to capture key conformational substates along the activation pathway for the purpose of allosteric drug designing^{23–25}.

Computational methods, especially molecular dynamics (MD) simulations, have become a well-established technique for investigating the conformational landscapes of GPCRs at an atomic level and uncovering biomolecular mechanisms that are unattainable by experimental methods^{26–33}. Integrating MD simulations with Markov state models (MSMs)^{34–36} has proven successful in understanding the molecular switches in β_2 adrenergic receptor,³⁷ elucidating ligand-driven conformational changes in CC chemokine receptor 2³⁸, and revealing a cryptic pocket in dopamine D3 receptor³⁹.

Here, we use a computational framework that includes a transition pathway generation algorithm, extensive all-atom MD simulations (300 μ s) of AT1R in the membrane-embedded environment, and MSM analysis for investigating the conformational landscapes of AT1R activation. Our study not only offers a deep atomic-

level insight into AT1R activation, but also provides an opportunity for the design of allosteric AT1R modulators.

Results

Activation pathway of AT1R was discovered via extensive unbiased MD simulations

To understand the inactive-to-active conformational transition pathway of AT1R, we first generated a minimum energy path (MEP) by connecting the starting, inactive (PDB ID: 4YAY) and the end, active (PDB ID: 6DO1) states by inserting a series of replicas using the string method with the nudged elastic band (NEB) method (see Materials and Methods). After a simulated annealing process, 15 initial structures distributed on the MEP were selected and subsequently embedded with 1-palmitoyl-2-oleoyl-*sn*-glycero-3-phosphocholine (POPC) membrane and explicit water. Each structure had $2 \mu\text{s} \times 10$ independent runs with random initial velocities, leading to a cumulative simulation timescale of 300 μs . Such an extensive timescale has been proven efficient for exploring the GPCR activation process^{21,40}. As shown in Fig. 1, the most remarkable TM domain conformational variations of AT1R during activation are arguably the outward movements of TM5 and TM6, and the inward displacement of TM7. Thus, we defined two activation parameters, as shown in Fig. 1C, to project the simulated trajectories onto a two-dimensional (2D) space to comprehensively capture the conformational landscape of AT1R activation. Notably, L^{5.55} (superscripts indicate the Ballesteros-Weinstein numbering for GPCR residues)⁴¹ undergoes a large and conserved rearrangement during GPCR activation and N^{7.46} occupies a highly conserved NPxxY motif on TM7.^{42,43} Thus, one parameter for defining activation was the distance between the C α atoms of L^{5.55} and N^{7.46}, which represented the conformational changes of TM5 and TM7. The other parameter was the angle between the C α atoms of F^{6.34}, S^{6.47}, and V^{2.41}, which reflected the outward movement of TM6; this is a crucial hallmark of GPCR activation that provides space to accommodate downstream signal proteins such as G proteins or β -arrestins^{42,44}. As shown in Fig. 1C, the corresponding distance and angle values were markedly distinct between the inactive and active AT1R crystal structures, thereby highlighting the differential ability of the activation parameters.

Based on these activation parameters, we calculated the corresponding value of each

point during the simulations and plotted a free-energy landscape (Fig. 2A), depicting the inactive-to-active transition pathway of AT1R activation. Because the initial inactive crystal structure of AT1R was located at a distance and angle of 21.3 Å and 36.7°, respectively, the largest free energy basin with a distance of ~19–23 Å and an angle of ~35–42° represented the inactive region. Further, because of the outward movement of TM6, the angle gradually increased, reflecting an open degree of TM6; whereas the movement of TM5 and TM7 caused a decrease in the interhelical distance. During the activation process, AT1R overcomes a relatively low energy barrier and enters the intermediate state located at a free energy basin with a distance of ~17–19 Å and an angle of ~46–51°, and it then crosses a high energy barrier at ~17 Å and 63° to arrive at the active state (17.4 Å, 69.4°), i.e., the coordinate of the active crystal structure. Overall, the convergence of the landscape was proven in both the timescale of a single trajectory and the number of rounds (see Section 1 of the Supporting Information, SI), confirming that the sampling was sufficient to explore AT1R activation.

Because of the recent breakthroughs in receptor engineering and crystallization, more than 300 class A GPCR structures of >50 receptors have been determined by X-ray and cryo-EM crystallography (Section 2, SI). These structures represent the GPCR conformational ensemble covering all inactive, active, and intermediate states, including different *apo* or antagonist-bound inactive conformations, agonist-bound multiple (intermediate, “active-like,” and active) conformations, and their effector G-protein- or β -arrestin-bound active conformations. Considering the conformational heterogeneity of class A GPCR structures, we projected these experimentally solved structures onto the 2D conformational landscape of AT1R sampled by simulations. The corresponding residues at positions 5.55, 7.46, 6.34, 6.47, and 2.41 of each structure were selected to calculate the distance and angle using their C α atoms. The active, inactive, and intermediate states defined by GPCRdb⁴⁵ database were mapped onto the 2D landscape of AT1R to provide insights into the dynamic conformational landscape of the receptors. As shown in Fig. 2B, the projection suggests that the AT1R activation pathway samples a wide conformational landscape of GPCR ensemble with the major distribution of experimental structures within the reaction path; this suggests that the computational model is in reasonable agreement with the experimental data. Together, the agreements between the simulated and

experimental data highlight the ability of our simulations to reproduce the overall GPCR activation, and suggest that it is thus suitable for further investigations.

Interestingly, the inactive energy basin largely matched its crystal and cryo-EM structures. This is probably ascribed to the fact that the inactive receptor structures are relatively stable and the conformer of crystallization is close to its energy basin. In contrast, due to their instability, the active state of GPCRs requires downstream effector G-proteins or G-protein mimetic nanobodies to stabilize the receptor conformational states during crystallization, inducing a part of the active structures (mostly rhodopsin receptor, Section 2, SI) that are located at ~ 22 Å and 65° . Such a deviation represents the instability of the active GPCR structures determined by experiments. However, many of them still occupy the area in the vicinity of the energy basin, and the angle parameter matches the distribution of the active structures well. Collectively, the free-energy landscape illustrates the activation process of AT1R and uncovers a hidden intermediate state along the pathway linking the inactive and active receptors.

Markov State Model revealed a synergistic transition mechanism of AT1R activation

To elucidate the mechanism of AT1R activation, we built a kinetic network Markov state model (MSM) using the activation parameters. From a statistical viewpoint, MSM provides summarized insights of the conformational ensemble of biomacromolecules at equilibrium. As such, the key intermediate states are identified more precisely, and the thermodynamic properties, such as transition timescale, are also quantified.^{34,37} Upon the validation of the Markovian properties by implied timescale test (Section 3, SI), we constructed a 200-microstate MSM using the k-means algorithm and clustered them into three macrostates, as shown in Fig. 3A, according to the conformer proportion. Then, transition path theory (TPT) mapped out the transitions and their timescales among the active, inactive, and intermediate states (Fig. 3B). The prediction of MSMs in the three macrostates was also confirmed by the Chapman–Kolmogorov test (Section 3, SI).

As shown in Fig. 3A, the whole conformational space was divided into three regions, and the locations of yellow, green, and purple regions corresponded to inactive, active, and intermediate states, respectively. Thus, the population ensemble determined by the 3-macrostate MSM was consistent with our state distribution. Notably, the proportion of the

inactive state (43.1%) was the largest in the ensemble; this is consistent with the fact that the *apo* AT1R naturally stays in the inactive state. However, because of the existence of basal activity, the active state also occupied 28.1% of the conformations during simulation, indicating that the *apo* AT1R still had a certain ability to trigger downstream pathways.

The transition from the inactive to the active states (401.63 μ s) was significantly longer than the transition from the active to inactive states (266.84 μ s), as shown in the transition timescale in Fig. 3B. This observation supports the notion that the *apo* AT1R is normally inactive but the active conformer also exists in its ensemble, which is in line with the basal activity in GPCR^{46–48}. Based on the AT1R conformational distribution, it is evident that both the active (86.46 μ s) and inactive (93.95 μ s) states were more amenable to transfer to the intermediate state. However, it was difficult for the intermediate state to transfer to the active state (257.87 μ s) and the inactive state (125.66 μ s). As a result, the kinetics of the activation pathway indicated that the rate-limiting step of AT1R activation was the transition from the intermediate to the active states.

To further elucidate the activation mechanism of AT1R, we focused on the observation of the key residue rearrangements. During GPCR activation, the emergence of residue rearrangements or “micro-switches” is fundamental to TM movement.^{42,49} Common activation micro-switches include the breaking of hydrophobic lock composed of residue positions 3.43, 6.40, and 6.41, which loosens the connection between TM3 and TM6, and the rupture of a conserved “ionic lock” between residue positions 3.50 and 6.30, which releases TM6 outwards^{42,50}. In addition, AT1R harbors some unique residue movements as well. In the inactive state, R^{3.50} and N^{6.30} form a relatively weak polar interaction instead of the conserved ionic lock and break upon activation. Further, F^{6.44} and F^{6.45} ratchet over F^{5.51} when AT1R is activated. Additionally, Y^{7.53} and Y^{5.53} tend to approach each other during AT1R activation, which reflects the movement of TM5 and TM7²⁰.

Using the Robust Perron Cluster Cluster Analysis (PCCA+) algorithm, we clustered the representative conformations of the macrostates (Fig. 4A–C). The micro-switches are also shown in the inactive, intermediate, and active AT1R states. Based on a representative simulation trajectory across the three states, we observed the dynamic situation of our switches (Fig. 4D–F). Globally, TM6 moved outwards, while TM5 and TM7 approached

the inactive-to-active conformational transition. Meanwhile, the landscape coordinates of the inactive, intermediate, and active representative conformations were located at (23.3 Å, 40.3°), (19.0 Å, 50.6°), and (17.1 Å, 71.3°), respectively; this greatly matched the low-energy conformer and further strengthened the accuracy and rationality of our cluster methodology.

Other structural elements are also worth mentioning. Upon activation, ECL2 moved towards the center of the endogenous AngII pocket and nearly closed the pocket in the active state, indicating that ECL2 stabilizes the pocket and maintains the binding of AngII during activation. Moreover, intracellular TM5 formed more α -helices in the active state, and the length of ICL2 decreased correspondingly. This helps in the binding of the downstream proteins, and is in line with the common GPCR activation process. In addition, H8 moved upward from the inactive to the active state to provide space for the downstream effectors. This upward movement may offer an opportunity for the formation of a “cryptic” pocket, which may be used for drug design.

We further identified different secondary structural elements in each macrostate, using the Definition of Secondary Structure of Proteins (DSSP) algorithm (Section 4, SI), to estimate the variations in the structures. Overall, AT1R maintained its seven helical architecture, and the macrostates showed limited fluctuation when compared with themselves; this confirmed the accuracy of our classification. However, the active AT1R had a more stable ECL2 between TM4 and TM5 than both the inactive and intermediate states, thereby suggesting that the active AT1R closes the endogenous pocket better. Between TM5 and TM6, the elongation of the intracellular α -helix of TM5 positioned ICL3 in the active state. However, this part of the residue was interchanged between the α -helix, β -bend, and loop in the intermediate state. Hence, the intermediate AT1R is involved in the transition process of activation. Additionally, the boundary between TM7 and H8 was vague in the inactive state. This implies that the angle between TM7 and H8 increases and that H8 moves towards the inactive state, which is also in line with the observation of the representative structures. These key domain movements and structural variations are synergistic from the inactive to the intermediate and active states, and thus suggest a synergistic mechanism for AT1R activation.

In agreement with the observations revealed by comparing the crystal structures, the

micro-switches generally and synergistically changed from the inactive state to the intermediate and active states. For example, V^{6.41} moved towards the membrane step-by-step and finally broke the hydrophobic lock in the active structure. This movement provided space for Y^{7.53}, which finally approached Y^{5.58}. In addition, the distance between R^{3.50} and N^{6.30} increased upon the outward movement of TM6, which in turn, rendered F^{6.44} and F^{6.45} to ratchet over F^{5.51}. Meanwhile, the relative positions of the residues in the intermediate state were in between the active and inactive states, indicating that the activation process occurs generally. In a single spontaneous activation trajectory, as shown in Fig. 4D–F, the variations of the three micro-switches (breaking of the ionic lock in Fig. 4D, opening of the “hydrophobic lock” in Fig. 4E, and rearrangement of phenylalanine ratchet in Fig. 4F) synchronize, and thus reflect the synergistic activation mechanism of AT1R. Thus, the zoom-in views of the residue rearrangements were consistent with the global secondary structural movements.

We also applied community analysis to elucidate the signal transduction in different states of AT1R. The global complexity of connection was decreased upon activation, but the key interactions among the areas were promoted in the active state (Section 5, SI). For instance, the connections between C3 (intracellular TM3 and TM5), C4 (ICL2 and around TM5 and TM6), and C5 (intracellular TM2 and TM4), which represent the interaction of the transducer pocket with other AT1R regions, were enhanced in the active state. This implies that some unnecessary interactions are quenched during activation, but the connections that transmit the effect of the agonist are maintained. The absence of interactions between C4 and C5 in the intermediate state may reflect a transition state to form new connections. In addition, H8 was not an individual community in the active AT1R but merged itself with TM1, which reflects that it couples with other parts more during activation.

Biased signaling was observed in two distinct active conformations

Apart from the dimension reduction accomplished by the features extracted from the biological process (e.g., our activation parameters shown in Fig. 1C), we also applied time-structure-based independent component analysis (tICA) to our system to analyze the global movement of information during activation. tICA employs linear combinations to

particular features, such as the phi/psi angle of the backbone, to maximize the decorrelation time among these features. Thus, tICA enables the capture of slow dynamic processes during simulations^{34,51,52}. With the help of tICA, we projected the trajectories onto another 2D landscape, which was representative of the global phi/psi movement. Through the implied timescale test, dimensionality reduction using tICA has been proven to have Markovian properties. The tICA landscape was separated into eight macrostates according to the PCCA+ algorithm, and its prediction met the requirements of the Chapman–Kolmogorov test (Section 6, SI). To analyze the global movement during simulations, the representative conformations of each tICA macrostate were extracted and projected onto the distance-angle landscape based on their corresponding activation parameters (Fig. 5A). Finally, the TPT method was applied to calculate the transition dynamics between six major macrostates (Fig. 5B).

As shown in Fig. 5A, macrostates 1 and 5 were in the intermediate state, macrostates 2–4 and 8 in the inactive state, and macrostates 6 and 7 in the active state. Notably, the macrostates 3–8 occupied more than 96% of the snapshots during our simulations (Section 6, SI) and stayed close to the energy basins in our landscape (Fig. 2A), thereby suggesting that the coordinate parameters (distance and angle) elucidated the activation process just as the global movement did. Thus, the mechanism according to the activation parameters is credible. In addition, the representative conformations of macrostates 4 and 6 corresponded to the area with the most inactive and active crystal structures, respectively (Fig. 2B and 5A). A recent study has stated that a conformation similar to the active structure of GPCRs that interacts with G-proteins is referred to as the “canonical active” conformation²⁷. Meanwhile, pathway 4–5–6 took the shortest transition time, thus it is the most preferential way to activate AT1R among all the analyzed pathways (Fig. 5B). Thus, macrostates 4 and 6 are crucial conformers along the activation pathway; that is, macrostate 4 is encountered before entering the activation process, and the typical activation process involves the macrostates 4–6. According to the definition of the canonical active conformation, macrostate 6 has the potential to be canonical during activation²⁷.

AT1R exerts its cellular and physiological functions mainly through the Gq-mediated pathway. The receptor is phosphorylated at its C-terminus by G protein-coupled receptor

kinases, which promote the recruitment of β -arrestins. The β -arrestins desensitize the receptor, but also mediate G protein-independent signaling by scaffolding or allosterically regulating the downstream signaling molecules⁵³⁻⁵⁶. AT1R harbors canonical and alternative active conformations to interact with the G-proteins and β -arrestins, respectively. Different ligands induce different conformations, which leads to a biased signaling²⁷. Since both macrostates 6 and 7 were defined as active states, we modeled the structural binary complexes of different AT1R-Gq and AT1R- β -arrestin based on the availability of the GPCR-transducer structures (Fig. 6; also see Section 7, SI) to determine whether the two active conformations had a bias for the transducers, i.e., G-protein versus β -arrestin.

As shown in Fig. 6, the macrostates 6 and 7 corresponded to the canonical and alternative active conformations, respectively. In macrostate 6, the sidechain of R^{3.50} of AT1R was horizontal, and accommodated the $\alpha 5$ helix of the Gq protein. In sharp contrast, R^{3.50} in macrostate 7 tilted towards the intracellular side and clashed with the Gq protein. As a result, macrostate 7 was resistant to binding to Gq protein, and this corresponds with the definition of the alternative active conformation. Indeed, the two macrostates are suitable for β -arrestin binding. Thus, we clearly showed that both the canonical and alternative active conformations exist in *apo* AT1R. During biased signaling, different ligands stabilize distinct receptor conformers; this reflects that the biased signaling of AT1R occurs via a conformational selection mechanism. Taken together, tICA identified a transition pathway based on global movements, and the two active conformations provided indications of biased signaling.

Identification of a cryptic allosteric site in the intermediate state

We also utilized a pocket prediction algorithm to represent the structures of the macrostates and guide the allosteric drug design. Using Fpocket, we identified and clustered nine pockets on the hidden intermediate state (Fig. 3A) and several pockets in other states. In Fig. 7A and Section 8, SI, the positions of the pockets are depicted and the overlapping pockets between the intermediate state and other states are also highlighted. Most of the detected pockets in the intermediate state corresponded to pockets in the inactive and active states, except for P6 and P9, which were the cryptic pockets that were visible only

in the intermediate state.

Among the nine pockets, P1 was located at the center of AT1R and spanned from top to bottom. It revealed a large cavity inside AT1R and partly overlapped with the orthosteric site for AngII. Nevertheless, P1 was too large for the design of small-molecule modulators. In addition, pockets P2–P6 lay on the membrane side, whereas the intracellular P7–P9 pockets were in the proximity of the transducer site (Fig. 7A). The volume of pockets P2–P9 could fit possible allosteric modulator sites, and P2, P4, P8, and P9 matched previous allosteric drug sites as well (Fig. 7B and 7C). In particular, P2 was mostly identical to LY2119620 in M2 muscarinic acetylcholine receptor (M2R; PDB ID: 4MQT)⁵⁷. P8 also partially overlapped with the allosteric agonist AP8 in free fatty acid receptor 1 (GPR40; PDB ID: 5TZY)⁵⁸. In addition, BPTU interact with P2Y₁R (PDB ID: 4XNV)⁵⁹ in the vicinity of P4, confirming the accuracy of our site prediction. P9 overlapped with three allosteric sites observed in GPCR-modulator structures as an intermediate-only potential pocket. The sites were: CCR2-RA-[R] site in CC chemokine receptor 2 (CCR2; PDB ID: 5T1A), a vercirnon site in CC chemokine receptor 9 (CCR9; PDB ID: 5LWE), and Cmp-15PA site in β_2 AR (PDB ID: 5X7D), and were not confined to the intermediate state^{60–62}. Thus, P9 is a common allosteric site but not a novel site in the intermediate state of AT1R. However, since P2, P4, P8, and P9 emerged as the allosteric sites in other class A GPCR-modulator structures, the sites shown in Fig. 7A are highly likely allosteric sites.

Since P9 was excluded because of its universality, P6 remained the only novel and cryptic allosteric site in the intermediate state. Naturally, we explored other GPCR intermediate structures (Section 2, SI) to investigate the existence of P6. As a result, P6 was discovered in six structures, and three of them are shown in Fig. 8. The structures of GPCRs were close to those of intermediate AT1R, especially the angles of TM7 and H8. The pockets were also highly similar in their positions. As P6 has never been reported in previous GPCRs and allosteric modulator structures, our findings indicate that it may be a novel allosteric site for drug design.

Mutagenesis confirmed the predicted cryptic binding site

We corroborated that P6 was a novel site using clustered alanine-scanning mutagenesis. Five groups of mutants (Fig. 9A) were developed independently to investigate the effect

of allosteric perturbations of P6 on the activity of AT1R. The cluster 1 mutants included F^{1.48}A, L^{1.52}A, and I^{1.57}A, located on the intracellular side of TM1. The cluster 2 mutants were M57A, K58A, and K60A on ICL1. The cluster 3 mutant on the intracellular TM2 consisted of T^{2.37}A, S^{2.40}A, and L^{2.43}A. Further, the cluster 4 (N^{7.49}A, P^{7.50}A, and F^{7.55}A) and 5 (K^{8.49}A, F^{8.50}A, K^{8.51}A, Y^{8.53}A, and F^{8.54}A) mutants were on the pocket side of the angle formed by TM7 and H8. First, we measured the surface expression of each of these cluster mutants in human embryonic kidney (HEK) 293 cells coexpressing β -arrestin-2 using whole-cell enzyme-linked immunosorbent assay (ELISA) assay, and observed that all these cluster mutants were expressed at comparable levels to the wild-type (WT) receptor (Section 9, SI). Thus, the variation in the downstream signaling was not caused by the change in AT1R expression level. Since AT1R acts as a model system for biased signaling, we further investigated whether these cluster mutations had effects on AngII-induced Gq activation as well as β -arrestin-2 recruitment using bioluminescence resonance energy transfer (BRET) assays⁶³. Upon AngII stimulation, the WT AT1R displayed a dose-dependent Gq activation and β -arrestin-2 recruitment. Intriguingly, while the cluster 1 mutants showed a 20–30% decrease in both β -arrestin-2 and Gq activation, the mutations in other clusters completely abolished the AngII-induced Gq activation and β -arrestin-2 recruitment. Thus, P6 has the potential to regulate the activity of AT1R through allosteric effects. Considering the shared existence of P6 in the class A GPCR family, it is possible to develop general allosteric modulators targeting P6 and regulating GPCR activation.

Discussion

GPCRs have gained increasing attention as therapeutic targets for the treatment of Alzheimer's disease, Parkinson's disease, schizophrenia, and other central nervous system disorders. Despite intensive research and accumulation of considerable amounts of structural and functional data⁶⁴, it is still challenging to completely understand the mechanism of GPCR activation, elucidate the complex signaling machines that can adopt a slew of distinct conformations to modulate multiple downstream signaling pathways (known as biased signaling), and design small-molecule allosteric modulators that can distinguish between closely related receptor subtypes^{1,18,65,66}. As a quintessential model system for GPCR research, AT1R not only shows biased signaling by regulating its

endogenous ligand AngII, but also shows great promise as a therapeutic target for treating hypertension. Recently, the antagonist-bound (inactive), AngII-bound, and biased agonist-bound (active) AT1R structures have been determined¹⁹⁻²¹, yet, the dynamic process of receptor activation and its biased signaling through a conformational selection mechanism are still not fully understood^{8,67}.

In the present study, we employed extensive MD simulations (300 μ s) of AT1R and used the NEB method to define a pathway from the inactive to the active state. A free-energy landscape was identified and confirmed by MSM by referring to the common GPCR activation properties. MSM extracted representative conformations of the inactive, intermediate, and active states; consequently, a synergistic activation mechanism was proposed by comparing these conformations. Then, tICA was applied to analyze the global movement, and it identified distinct active states that were biased for G-protein and/or β -arrestin. Between TM7 and H8, a cryptic allosteric site was discovered in the intermediate state and confirmed by site-directed mutagenesis. Cumulatively, our simulations and experiments make a significant contribution to literature as it provides insights into the AT1R activation mechanism and firstly discovered a novel allosteric pocket.

In general, the activation mechanism of AT1R is similar to that of the other class A GPCRs. During activation, TM6 moves outwards to provide space for the transducers, and TM5 and TM7 approach to form the pocket. Notably, H8 experiences an upward movement that creates a cryptic allosteric site during transition^{17,42}. However, AT1R has several other unique properties, upon activation, due to its unique residue composition. For instance, R^{3.50} and N^{6.30} show weak polar interactions rather than a strong ionic lock as observed in other GPCRs; these facilitate the conformational rearrangements of TM6 to engage with the downstream effectors and increase the proportion of the active conformations in the *apo* ensemble²⁰. Interestingly, the approach of Y^{7.53} and Y^{5.58} promotes the formation of the active state, which is unique to AT1R. Thus, AT1R harbors a common activation mechanism, but also maintains its uniqueness in particular residue movement.

Notably, intermediate states and active states exist naturally in *apo* AT1R. This population distribution has been proven in other *apo* GPCRs as means of basal activity^{47,48,68,69}. Thus, agonists select and stabilize the active conformation of GPCRs and

promote the binding of transducers. Once the transducers bind with the GPCRs, the active conformation harbors lower energy, hereafter the fully stabilized active state^{44,69,70}, and proves the conformational selection mechanism of GPCR activation. The active AT1R showed two distinct conformations, as determined by tICA, and thus supports the notion that both the canonical and alternative active conformations exist in the ensemble of AT1R. The two conformers are stabilized by G-protein and β -arrestin biased agonists, respectively²⁷, suggesting a population shift mechanism in the biased signaling^{71,72}. In contrast, the balanced agonists equally stabilize the two conformers, and thus lead to no preference for the downstream proteins⁴⁷. Thus, the emergence of biased signaling occurs via a conformational selection mechanism. In other words, the regulation of GPCR activity is attributed to a generalized allosteric modulation^{73,74}.

As GPCR regulation is an allosteric process, it is natural to design modulators targeting allosteric sites other than endogenous orthosteric sites⁷⁵. In the intermediate state, we discovered P6 as a novel site for allosteric regulation. Hidden between TM7 and H8, P6 was only observed during the upward movement of H8. Community analysis reflected that the impeding signal transmission between H8 and other parts impeded the formation of an active conformation. As a novel pocket, P6 has not emerged in current GPCR-ligand crystal structures but has been identified in other intermediate structures^{8,76}. Hence, to our knowledge, this is the first time to discover a novel GPCR allosteric pocket in the membrane side of H8. Alanine-scanning experiments further confirmed that the residues around P6 transmit signals to modulate both G-protein and β -arrestin, and suggest that the allosteric perturbation from P6 has the potential to modulate the activity of AT1R. Many GPCRs currently lack features of endogenous ligands to initiate specific biased signaling. Hence, directly targeting intracellular TMs (such as P6) by allosteric modulators may provide a strategy to selectively regulate the GPCRs^{47,77}. Thus, as an unexploited allosteric site, P6 can be targeted in future allosteric drug designs for GPCRs. In order to fully realize P6 as a novel allosteric target for GPCRs, further structure-based drug design methodology and experimental investigation will be deployed by means of lead compound identification and optimization. These studies are not only expected to provide insights into the activation mechanism of AT1R, but also offer versatile applications for GPCR biology, biophysics, and medicinal chemistry.

Methods

Setup for MD simulation systems

From the Protein Data Bank (PDB), we obtained the inactive AT1R structure (PDB ID: 4YAY) and active AT1R structure (PDB ID: 6DO1). In both structures, the truncated N-terminal, ECL2, and ICL3 were recovered by loop building program, according to the sequence of the wild-type AT1R. The co-crystallized apocytochrome b₅₆₂RIL was removed from 4YAY. The hydrogens were added, while the termini were capped with acetyl and methylamide groups. Referring to the common sequence, the 9-317 residues in 4YAY and 6DO1 were extracted as the input structures for the following processes.

NEB sampling

To characterize the activation process of AT1R, the NEB method, a compelling approach to determine the transition pathways among conformations, was carried out. During the NEB process, a series of replicas (or images) with the same composition but different atom coordinates are generated between the initial and final states. The replicas are linked to their nearest neighbors via elastic bands, in order to confirm that they are evenly distributed along the pathway and prevent them from directly sliding down to the energy basin^{78,79}. Consequently, the replicas constitute a certain pathway that connect the start and end conformations.

Then, a simulated annealing process was applied to the replicas to find an MEP between the fixed initial and final states. In this process, the elastic bands were denoted as $3 \times N_{\text{atoms}}$ dimensional vectors $[\mathbf{R}_0, \mathbf{R}_1, \dots, \mathbf{R}_N]$, corresponding to the pathway from the initial state \mathbf{R}_0 and end state \mathbf{R}_N . To avoid interference of spring forces caused by the restraints and potential forces caused by the force fields, a tangent vector $\boldsymbol{\tau}_i$ at each replica position was introduced. With respect to the energy of replica i (V_i) and its neighbors, $\boldsymbol{\tau}_i$ is defined in eq (1).

$$\boldsymbol{\tau}_i = \begin{cases} \mathbf{R}_{i+1} - \mathbf{R}_i, & V_{i+1} > V_i > V_{i-1} \\ \mathbf{R}_i - \mathbf{R}_{i-1}, & V_{i+1} < V_i < V_{i-1} \\ (\mathbf{R}_{i+1} - \mathbf{R}_i)\Delta V_i^{\max} + (\mathbf{R}_i - \mathbf{R}_{i-1})\Delta V_i^{\min}, & V_i > V_{i+1} > V_{i-1} \text{ or } V_{i+1} > V_{i-1} > V_i \\ (\mathbf{R}_{i+1} - \mathbf{R}_i)\Delta V_i^{\min} + (\mathbf{R}_i - \mathbf{R}_{i-1})\Delta V_i^{\max}, & V_i > V_{i-1} > V_{i+1} \text{ or } V_{i-1} > V_{i+1} > V_i \end{cases} \quad (1)$$

where $\Delta V_i^{\max} = \max(|V_{i+1} - V_i|, |V_{i-1} - V_i|)$
 $\Delta V_i^{\min} = \min(|V_{i+1} - V_i|, |V_{i-1} - V_i|)$

With $\boldsymbol{\tau}_i$, eq (2) and eq (3) define the perpendicular (F_i^\perp) and parallel (F_i^\parallel) components of the total force, respectively.

$$F_i^\perp = -\nabla V(P_i) + (\nabla V(P_i) \cdot \boldsymbol{\tau}_i) \cdot \boldsymbol{\tau}_i \quad (2)$$

$$F_i^\parallel = (F^s \cdot \boldsymbol{\tau}_i) \cdot \boldsymbol{\tau}_i \quad (3)$$

$$F^{\text{total}} = F_i^\perp + F_i^\parallel \quad (4)$$

$\nabla V(P_i)$ represents the gradient of the energy with respect to the atomic coordinates in replica i , namely the potential force originating from the force fields. F^s is the force provided by the elastic bands. As a result, the force field parameters only contribute to the perpendicular part of the total force, and the spring force is only responsible for the parallel part [eq (4)]^{80,81}.

After the preparation, the inactive (PDB ID: 4YAY) and active (PDB ID: 6DO1) structures were set as the initial and end states, respectively. The Amber ff14SB force field was adapted for atom interactions⁸². First, we conducted 4000 steepest descent and 6000 conjugate gradient energy minimization cycles to our two systems. Then, 20 replicas were created between the inactive and active AT1Rs with elastic bands connecting each other. The translational and rotational differences between the replicas were excluded by moving the systems to the coordinate of the center-of-mass and applying an optimal rotation matrix to the replicas to minimize the root mean square deviation (RMSD) between the systems. In the initial heating process, the systems were gradually heated from 0 K to 300 K with a spring force of $10 \text{ kcal mol}^{-1} \text{ \AA}^{-2}$, a timestep of 0.5 fs, and a Langevin collision frequency of 1000 ps^{-1} . During the next equilibration, simulated annealing, and cooling runs, a spring force of $50 \text{ kcal mol}^{-1} \text{ \AA}^{-2}$ was used. The equilibration runs of the replicas were carried out at 300 K with a timestep of 1 fs. In the simulated annealing runs, the systems were first heated to 500 K, then gradually cooled and equilibrated alternatively at 0 K with a timestep of 0.5 fs. Finally, the replicas were completely cooled at 0 K for 2 ns with a timestep of 1

fs. The detailed workflow has been delineated in previous studies^{23,78,83}.

MD simulation settings

The NEB process provided 22 replicas, but some had highly similar conformations. Thus, we calculated the RMSD between adjacent structures and accordingly selected the most different 15 replicas, including the starting and end structures, as the initial structures for the MD simulations.

All structures were oriented in the Orientations of Proteins in Membranes (OPM) server.⁸⁴ Next, they were inserted into a POPC membrane using the CHARMM36 additive force field in the CHARMM-GUI server⁸⁵. TIP3P water molecules with a length of 10 Å were added to the top and bottom of the system. The counterions K⁺ and Cl⁻ and an additional 0.15 mol/L KCl were also solvated in the systems. With the help of the input generator of CHARMM-GUI, we obtained the Amber format coordinate and topology files.

The systems were first minimized with a restraint of 500 kcal mol⁻¹ Å⁻² on AT1R and lipids, while water and counterions were minimized in 8000 steepest descent cycles, followed by 7000 conjugate gradient cycles. Second, all atoms encountered 1.5×10^4 cycles of steepest descent and 1.5×10^4 cycles of conjugate gradient minimization. Next, with a 10 kcal mol⁻¹ Å⁻² position restraint on proteins and lipids, the systems were gradually heated from 0 K to 300 K in 300 ps and equilibrated for 700 ps under NVT conditions. Then, the 15 systems underwent 10 rounds of 2 μs MD simulations, with an integration step of 2.0 fs. Finally, we collected 150 independent repeat trajectories with random initial velocities. The total simulation timescale was 300 μs. During simulations, the Particle mesh Ewald (PME) method was applied to calculate the long-range electrostatic interactions, and a cutoff of 10 Å was used for short-range electrostatic and van der Waals interactions⁸⁶. The SHAKE algorithm was employed for covalent bonds containing hydrogen⁸⁷. A temperature of 300 K was controlled by Langevin Thermostat, while the collision frequency was 1.0 ps⁻¹⁸⁸. The snapshots were written out every 200 ps.

Markov State Model construction

According to the activation parameters, an MSM was built using the PyEMMA protocol

(<http://www.emma-project.org/latest/>)⁸⁹. Through the implied timescale validation (Section 6, SI), we confirmed that the AT1R systems were Markovian and reliable with a 200 microstate model with a lag time of 8 ns and a maximum k-means iteration number of 200. Then, the microstates were clustered into three macrostates via the PCCA+ algorithm, which was confirmed by a Chapman–Kolmogorov test. Using TPT, we measured the transition probability matrix of the MSMs and computed the mean first passage time (MFPT) for each activation and inactivation process⁹⁰. Based on the “mdtraj” package, we extracted the structures close to the microstate cluster centers of each macrostate into trajectories for the corresponding macrostates. Then, using three trajectories, we selected the representative conformation of each macrostate according to the similarity score S_{ij} . As shown in eq (5), the conformation with the highest S_{ij} among the trajectories was regarded as the most representative conformation of the macrostate. The d_{ij} is the RMSD between the conformations i and j , while d_{scale} is the standard deviation of d ⁹¹. Finally, Fpocket was applied to discover the pockets on the conformations⁹².

$$S_{ij} = e^{-d_{ij}/d_{scale}} \quad (5)$$

Site-directed mutagenesis

Cluster mutations of AT1R (cluster 1: F44A/L48A/I53A; cluster 2: M57A/K58A/K60A; cluster 3: T61A/S64A/L67A; cluster 4: N298A/P299A/F304A; and cluster 5: K308A/F309A/K310A/Y312A/F313A) were generated by site-directed mutagenesis. The successful mutations in the polymerase chain reaction products were verified by DNA sequencing.

BRET measurement

(1) β -arrestin-2 recruitment

HEK293 cells were transiently co-transfected with β -arrestin-2-Rluc and AT1R-yellow fluorescent protein (AT1R-YFP). Twenty-four hours after transfection, the cells were distributed in a 96-well microplate. After another 24 h incubation at 37 °C, the cells were washed twice with Hank’s balanced salt solution (HBSS) and stimulated with AngII at different concentrations. Luciferase substrate was added and then light emissions were recorded using a Mithras LB940 microplate reader (Berthold Technologies). The BRET

signal was determined by calculating the ratio of luminescence at 530 nm/485 nm.

(2) Gq protein activation

Gq BRET probes were generated according to a previous report⁹³. HEK293T cells were transiently co-transfected with AT1R and Gq BRET probes. Twenty-four hours after transfection, the cells were distributed into a 96-well microplate for an additional 24 h. The cells were washed twice with HBSS and stimulated with AngII at different concentrations. The BRET signal was measured after the addition of the luciferase substrate using a Mithras LB940 microplate reader. The BRET signal was calculated as the ratio of light emission at 510 nm/400 nm.

Supporting information

The Supporting Information includes the convergence test, validation of MSMs, analysis of known class A GPCR structures, dynamic properties of different macrostates, tICA analysis and its validation, the alignment of AT1R-transducers, in-detail pocket positions, as well as the measurement of mutant AT1R expression.

Acknowledgements

This work was supported in part by grants from the National Natural Science Foundation of China (22077082, 21778037, 81925034, 91753117, and 81721004), the Innovation Program of Shanghai Municipal Education Commission (2019-01-07-00-01-E00036, China), the Shanghai Science and Technology Innovation (19431901600, China), and the Shanghai Health and Family Planning System Excellent Subject Leader and Excellent Young Medical Talents Training Program (2018BR12, China).

Declaration of competing interests

The authors declare no conflicts of interest.

Author contributions

S.L. and J.Z. conceived and supervised the project. S.L., J.Z., and J.S. designed the experiments and revised the manuscript. X.H. and Z.Y. designed and performed the

experiments, and drafted the manuscript. X.H. contributed to MD and analysis. Z.Y. and J.W. acquired and analyzed BRET data. T.Z., A.R., D.N., and J.P. acquired data and revised the manuscript. S.L., J.Z., and J.S. were responsible for conception and oversight of the project. All authors discussed the results and reviewed the manuscript.

References

1. Hauser, A. S., Attwood, M. M., Rask-Andersen, M., Schiöth, H. B. & Gloriam, D. E. Trends in GPCR drug discovery: new agents, targets and indications. *Nat. Rev. Drug Discov.* **16**, 829–842 (2017).
2. Hutchings, C. J., Koglin, M., Olson, W. C. & Marshall, F. H. Opportunities for therapeutic antibodies directed at G-protein-coupled receptors. *Nat. Rev. Drug Discov.* **16**, 787–810 (2017).
3. Venkatakrisnan, A. J. *et al.* Molecular signatures of G-protein-coupled receptors. *Nature* **494**, 185–194 (2013).
4. Weis, W. I. & Kobilka, B. K. The Molecular Basis of G Protein–Coupled Receptor Activation. *Annu. Rev. Biochem.* **87**, 897–919 (2018).
5. Flock, T. *et al.* Universal allosteric mechanism for G α activation by GPCRs. *Nature* **524**, 173–179 (2015).
6. Seyedabadi, M., Ghahremani, M. H. & Albert, P. R. Biased signaling of G protein coupled receptors (GPCRs): Molecular determinants of GPCR/transducer selectivity and therapeutic potential. *Pharmacol. Ther.* **200**, 148–178 (2019).
7. Changeux, J.-P. & Christopoulos, A. Allosteric Modulation as a Unifying Mechanism for Receptor Function and Regulation. *Cell* **166**, 1084–1102 (2016).
8. Lu, S. & Zhang, J. Small Molecule Allosteric Modulators of G-Protein-Coupled Receptors: Drug–Target Interactions. *J. Med. Chem.* **62**, 24–45 (2019).
9. Nussinov, R. & Tsai, C.-J. Allostery in Disease and in Drug Discovery. *Cell* **153**, 293–305 (2013).
10. Foster, D. J. & Conn, P. J. Allosteric Modulation of GPCRs: New Insights and Potential Utility for Treatment of Schizophrenia and Other CNS Disorders. *Neuron* **94**, 431–446 (2017).
11. Lu, S., Shen, Q. & Zhang, J. Allosteric Methods and Their Applications:

- Facilitating the Discovery of Allosteric Drugs and the Investigation of Allosteric Mechanisms. *Acc. Chem. Res.* **52**, 492–500 (2019).
12. Lindsley, C. W. *et al.* Practical Strategies and Concepts in GPCR Allosteric Modulator Discovery: Recent Advances with Metabotropic Glutamate Receptors. *Chem. Rev.* **116**, 6707–6741 (2016).
 13. Xiang, J. *et al.* Successful Strategies to Determine High-Resolution Structures of GPCRs. *Trends Pharmacol. Sci.* **37**, 1055–1069 (2016).
 14. Congreve, M., Oswald, C. & Marshall, F. H. Applying Structure-Based Drug Design Approaches to Allosteric Modulators of GPCRs. *Trends Pharmacol. Sci.* **38**, 837–847 (2017).
 15. Zhao, S., Wu, B. & Stevens, R. C. Advancing Chemokine GPCR Structure Based Drug Discovery. *Structure* **27**, 405–408 (2019).
 16. Shi, Y. A glimpse of structural biology through X-ray crystallography. *Cell* **159**, 995–1014 (2014).
 17. Latorraca, N. R., Venkatakrisnan, A. J. & Dror, R. O. GPCR dynamics: structures in motion. *Chem. Rev.* **117**, 139–155 (2016).
 18. Maning, J., Negussie, S., Clark, M. A. & Lymperopoulos, A. Biased agonism/antagonism at the AngII-AT1 receptor: Implications for adrenal aldosterone production and cardiovascular therapy. *Pharmacol. Res.* **125**, 14–20 (2017).
 19. Zhang, H. *et al.* Structure of the angiotensin receptor revealed by serial femtosecond crystallography. *Cell* **161**, 833–844 (2015).
 20. Wingler, L. M., McMahon, C., Staus, D. P., Lefkowitz, R. J. & Kruse, A. C. Distinctive Activation Mechanism for Angiotensin Receptor Revealed by a Synthetic Nanobody. *Cell* **176**, 479–490 (2019).
 21. Wingler, L. M. *et al.* Angiotensin and biased analogs induce structurally distinct active conformations within a GPCR. *Science.* **367**, 888–892 (2020).
 22. Wingler, L. M. *et al.* Angiotensin Analogs with Divergent Bias Stabilize Distinct Receptor Conformations. *Cell* **176**, 468-478.e11 (2019).
 23. Lu, S. *et al.* Deactivation Pathway of Ras GTPase Underlies Conformational Substates as Targets for Drug Design. *ACS Catal.* **9**, 7188–7196 (2019).

24. Shukla, D., Meng, Y., Roux, B. & Pande, V. S. Activation pathway of Src kinase reveals intermediate states as targets for drug design. *Nat. Commun.* **5**, 3397 (2014).
25. Curado-Carballada, C., Feixas, F., Iglesias-Fernández, J. & Osuna, S. Hidden Conformations in *Aspergillus niger* Monoamine Oxidase are Key for Catalytic Efficiency. *Angew. Chemie - Int. Ed.* **58**, 3097–3101 (2019).
26. Zhang, M., Jang, H. & Nussinov, R. The mechanism of PI3K α activation at the atomic level. *Chem. Sci.* **10**, 3671–3680 (2019).
27. Suomivuori, C.-M. *et al.* Molecular mechanism of biased signaling in a prototypical G protein-coupled receptor. *Science.* **367**, 881–887 (2020).
28. Mattedi, G., Acosta-Gutiérrez, S., Clark, T. & Gervasio, F. L. A combined activation mechanism for the glucagon receptor. *Proc. Natl. Acad. Sci. U. S. A.* **117**, 15414–15422 (2020).
29. Bhattarai, A., Devkota, S., Bhattarai, S., Wolfe, M. S. & Miao, Y. Mechanisms of γ -Secretase Activation and Substrate Processing. *ACS Cent. Sci.* **6**, 969–983 (2020).
30. Guros, N. B., Balijepalli, A. & Klauda, J. B. Microsecond-timescale simulations suggest 5-HT-mediated preactivation of the 5-HT_{3A} serotonin receptor. *Proc. Natl. Acad. Sci. U. S. A.* **117**, 405–414 (2020).
31. Chan, H. C. S. *et al.* Enhancing the Signaling of GPCRs via Orthosteric Ions. *ACS Cent. Sci.* **6**, 274–282 (2020).
32. Zhang, H. *et al.* Structural basis for selectivity and diversity in angiotensin II receptors. *Nature* **544**, 327–332 (2017).
33. Wu, M. *et al.* Molecular Mechanism of Acetate Transport through the Acetate Channel SatP. *J. Chem. Inf. Model.* **59**, 2374–2382 (2019).
34. Husic, B. E. & Pande, V. S. Markov State Models: From an Art to a Science. *J. Am. Chem. Soc.* **140**, 2386–2396 (2018).
35. Shukla, D., Hernández, C. X., Weber, J. K. & Pande, V. S. Markov state models provide insights into dynamic modulation of protein function. *Acc. Chem. Res.* **48**, 414–422 (2015).
36. Wang, W., Cao, S., Zhu, L. & Huang, X. Constructing Markov State Models to

- elucidate the functional conformational changes of complex biomolecules. *Wiley Interdiscip. Rev. Comput. Mol. Sci.* **8**, e1343 (2018).
37. Kohlhoff, K. J. *et al.* Cloud-based simulations on Google Exacycle reveal ligand modulation of GPCR activation pathways. *Nat. Chem.* **6**, 15–21 (2014).
 38. Taylor, B. C., Lee, C. T. & Amaro, R. E. Structural basis for ligand modulation of the CCR2 conformational landscape. *Proc. Natl. Acad. Sci. U. S. A.* **116**, 8131–8136 (2019).
 39. Ferruz, N. *et al.* Dopamine D3 receptor antagonist reveals a cryptic pocket in aminergic GPCRs. *Sci. Rep.* **8**, 1–10 (2018).
 40. Dror, R. O. *et al.* Activation mechanism of the β 2-adrenergic receptor. *Proc. Natl. Acad. Sci. U. S. A.* **108**, 18684–18689 (2011).
 41. Ballesteros, J. A. & Weinstein, H. Integrated methods for the construction of three-dimensional models and computational probing of structure-function relations in G protein-coupled receptors. in *Receptor Molecular Biology* (ed. Sealfon, S. C. B. T.-M. in N.) **25**, 366–428 (Academic Press, 1995).
 42. Zhou, Q. *et al.* Common activation mechanism of class A GPCRs. *Elife* **8**, e50279 (2019).
 43. Ragnarsson, L., Andersson, Å., Thomas, W. G. & Lewis, R. J. Mutations in the NPxxY motif stabilize pharmacologically distinct conformational states of the α (1B)- and β (2)-adrenoceptors. *Sci. Signal.* **12**, eaas9485 (2019).
 44. Rasmussen, S. G. F. *et al.* Crystal structure of the β 2 adrenergic receptor–Gs protein complex. *Nature* **477**, 549–555 (2011).
 45. Pándy-Szekeres, G. *et al.* GPCRdb in 2018: adding GPCR structure models and ligands. *Nucleic Acids Res.* **46**, D440–D446 (2018).
 46. Staus, D. P., Wingler, L. M., Pichugin, D., Prosser, R. S. & Lefkowitz, R. J. Detergent- and phospholipid-based reconstitution systems have differential effects on constitutive activity of G-protein-coupled receptors. *J. Biol. Chem.* **294**, 13218–13223 (2019).
 47. Wingler, L. M. & Lefkowitz, R. J. Conformational Basis of G Protein-Coupled Receptor Signaling Versatility. *Trends Cell Biol.* **30**, 736–747 (2020).
 48. Ye, L., Van Eps, N., Zimmer, M., Ernst, O. P. & Prosser, R. S. Activation of the

- A2A adenosine G-protein-coupled receptor by conformational selection. *Nature* **533**, 265–268 (2016).
49. Filipek, S. Molecular switches in GPCRs. *Curr. Opin. Struct. Biol.* **55**, 114–120 (2019).
 50. Tehan, B. G., Bortolato, A., Blaney, F. E., Weir, M. P. & Mason, J. S. Unifying family A GPCR theories of activation. *Pharmacol. Ther.* **143**, 51–60 (2014).
 51. Pérez-Hernández, G., Paul, F., Giorgino, T., De Fabritiis, G. & Noé, F. Identification of slow molecular order parameters for Markov model construction. *J. Chem. Phys.* **139**, 015102 (2013).
 52. Schwantes, C. R. & Pande, V. S. Modeling molecular kinetics with tICA and the kernel trick. *J. Chem. Theory Comput.* **11**, 600–608 (2015).
 53. Yang, F. *et al.* Allosteric mechanisms underlie GPCR signaling to SH3-domain proteins through arrestin. *Nat. Chem. Biol.* **14**, 876–886 (2018).
 54. Yang, F. *et al.* Phospho-selective mechanisms of arrestin conformations and functions revealed by unnatural amino acid incorporation and (19)F-NMR. *Nat. Commun.* **6**, 8202 (2015).
 55. Yang, Z. *et al.* Phosphorylation of G Protein-Coupled Receptors: From the Barcode Hypothesis to the Flute Model. *Mol. Pharmacol.* **92**, 201–210 (2017).
 56. Zhang, D.-L. *et al.* Gq activity- and β -arrestin-1 scaffolding-mediated ADGRG2/CFTR coupling are required for male fertility. *Elife* **7**, (2018).
 57. Kruse, A. C. *et al.* Activation and allosteric modulation of a muscarinic acetylcholine receptor. *Nature* **504**, 101–106 (2013).
 58. Lu, J. *et al.* Structural basis for the cooperative allosteric activation of the free fatty acid receptor GPR40. *Nat. Struct. Mol. Biol.* **24**, 570–577 (2017).
 59. Zhang, D. *et al.* Two disparate ligand-binding sites in the human P2Y1 receptor. *Nature* **520**, 317–321 (2015).
 60. Zheng, Y. *et al.* Structure of CC chemokine receptor 2 with orthosteric and allosteric antagonists. *Nature* **540**, 458–461 (2016).
 61. Oswald, C. *et al.* Intracellular allosteric antagonism of the CCR9 receptor. *Nature* **540**, 462–465 (2016).
 62. Liu, X. *et al.* Mechanism of intracellular allosteric β 2AR antagonist revealed by

- X-ray crystal structure. *Nature* **548**, 480–484 (2017).
63. Liu, C.-H. *et al.* Arrestin-biased AT1R agonism induces acute catecholamine secretion through TRPC3 coupling. *Nat. Commun.* **8**, 14335 (2017).
 64. Shimada, I., Ueda, T., Kofuku, Y., Eddy, M. T. & Wüthrich, K. GPCR drug discovery: integrating solution NMR data with crystal and cryo-EM structures. *Nat. Rev. Drug Discov.* **18**, 59–82 (2019).
 65. Jazayeri, A., Andrews, S. P. & Marshall, F. H. Structurally Enabled Discovery of Adenosine A(2A) Receptor Antagonists. *Chem. Rev.* **117**, 21–37 (2017).
 66. Zou, Y., Ewalt, J. & Ng, H.-L. Recent Insights from Molecular Dynamics Simulations for G Protein-Coupled Receptor Drug Discovery. *Int. J. Mol. Sci.* **20**, 4237 (2019).
 67. He, X., Ni, D., Lu, S. & Zhang, J. *Characteristics of allosteric proteins, sites, and modulators. Advances in Experimental Medicine and Biology* **1163**, (2019).
 68. Yin, Y. *et al.* Rearrangement of a polar core provides a conserved mechanism for constitutive activation of class B G protein-coupled receptors. *J. Biol. Chem.* **292**, 9865–9881 (2017).
 69. Hilger, D. *et al.* Structural insights into differences in G protein activation by family A and family B GPCRs. *Science*. **369**, eaba3373 (2020).
 70. Manglik, A. *et al.* Structural Insights into the Dynamic Process of β 2-Adrenergic Receptor Signaling. *Cell* **161**, 1101–1111 (2015).
 71. Tsai, C.-J. & Nussinov, R. A Unified View of “How Allostery Works”. *PLOS Comput. Biol.* **10**, e1003394 (2014).
 72. Kar, G., Keskin, O., Gursoy, A. & Nussinov, R. Allostery and population shift in drug discovery. *Curr. Opin. Pharmacol.* **10**, 715–722 (2010).
 73. Christopoulos, A. Advances in G protein-coupled receptor allostery: from function to structure. *Mol. Pharmacol.* **86**, 463–478 (2014).
 74. Wootten, D., Miller, L. J., Koole, C., Christopoulos, A. & Sexton, P. M. Allostery and Biased Agonism at Class B G Protein-Coupled Receptors. *Chem. Rev.* **117**, 111–138 (2017).
 75. Wu, Y., Tong, J., Ding, K., Zhou, Q. & Zhao, S. GPCR Allosteric Modulator Discovery. *Adv. Exp. Med. Biol.* **1163**, 225–251 (2019).

76. Massink, A., Amelia, T., Karamychev, A. & IJzerman, A. P. Allosteric modulation of G protein-coupled receptors by amiloride and its derivatives. Perspectives for drug discovery? *Med. Res. Rev.* **40**, 683–708 (2020).
77. Klein Herenbrink, C. *et al.* The role of kinetic context in apparent biased agonism at GPCRs. *Nat. Commun.* **7**, 10842 (2016).
78. Bergonzo, C., Campbell, A. J., Walker, R. C. & Simmerling, C. A Partial Nudged Elastic Band Implementation for Use with Large or Explicitly Solvated Systems. *Int. J. Quantum Chem.* **109**, 3781 (2009).
79. Jónsson, H., Mills, G. & Jacobsen, K. W. Nudged elastic band method for finding minimum energy paths of transitions. *Cl. Quantum Dyn Condens. Phase Simulations.* 385–404 (1997).
80. Henkelman, G. & Jónsson, H. Improved tangent estimate in the nudged elastic band method for finding minimum energy paths and saddle points. *J. Chem. Phys.* **113**, 9978–9985 (2000).
81. Ghoreishi, D., Cerutti, D. S., Fallon, Z., Simmerling, C. & Roitberg, A. E. Fast Implementation of the Nudged Elastic Band Method in AMBER. *J. Chem. Theory Comput.* **15**, 4699–4707 (2019).
82. Maier, J. A. *et al.* ff14SB: Improving the Accuracy of Protein Side Chain and Backbone Parameters from ff99SB. *J. Chem. Theory Comput.* **11**, 3696–3713 (2015).
83. Huang, M. *et al.* Conformational transition pathway in the activation process of allosteric glucokinase. *PLoS One* **8**, e55857 (2013).
84. Lomize, M. A., Pogozheva, I. D., Joo, H., Mosberg, H. I. & Lomize, A. L. OPM database and PPM web server: resources for positioning of proteins in membranes. *Nucleic Acids Res.* **40**, 370–376 (2012).
85. Jo, S. *et al.* CHARMM-GUI 10 years for biomolecular modeling and simulation. *J. Comput. Chem.* **38**, 1114–1124 (2017).
86. Darden, T., York, D. & Pedersen, L. Particle mesh Ewald: An $N \cdot \log(N)$ method for Ewald sums in large systems. *J. Chem. Phys.* **98**, 10089–10092 (1993).
87. Ryckaert, J. P., Ciccotti, G. & Berendsen, H. J. C. Numerical integration of the cartesian equations of motion of a system with constraints: molecular dynamics of

- n-alkanes. *J. Comput. Phys.* **23**, 327–341 (1977).
88. Adelman, S. A. & Doll, J. D. Generalized Langevin equation approach for atom/solid-surface scattering: General formulation for classical scattering off harmonic solids. *J. Chem. Phys.* **64**, 2375–2388 (1976).
 89. Scherer, M. K. *et al.* PyEMMA 2: A Software Package for Estimation, Validation, and Analysis of Markov Models. *J. Chem. Theory Comput.* **11**, 5525–5542 (2015).
 90. Chodera, J. D., Singhal, N., Pande, V. S., Dill, K. A. & Swope, W. C. Automatic discovery of metastable states for the construction of Markov models of macromolecular conformational dynamics. *J. Chem. Phys.* **126**, 155101 (2007).
 91. McGibbon, R. T. *et al.* MDTraj: A Modern Open Library for the Analysis of Molecular Dynamics Trajectories. *Biophys. J.* **109**, 1528–1532 (2015).
 92. Le Guilloux, V., Schmidtke, P. & Tuffery, P. Fpocket: an open source platform for ligand pocket detection. *BMC Bioinformatics* **10**, 168 (2009).
 93. Olsen, R. H. J. *et al.* TRUPATH, an open-source biosensor platform for interrogating the GPCR transducerome. *Nat. Chem. Biol.* **16**, 841–849 (2020).
 94. Shihoya, W. *et al.* Crystal structures of human ET(B) receptor provide mechanistic insight into receptor activation and partial activation. *Nat. Commun.* **9**, 4711 (2018).
 95. Yin, W. *et al.* Crystal structure of the human 5-HT(1B) serotonin receptor bound to an inverse agonist. *Cell Discov.* **4**, 12 (2018).
 96. Krumm, B. E., White, J. F., Shah, P. & Grisshammer, R. Structural prerequisites for G-protein activation by the neurotensin receptor. *Nat. Commun.* **6**, 7895 (2015).

Figures and Figure Legends

Figure 1. The distinction between inactive (PDB ID: 4YAY) and active (PDB ID: 6DO1) AT1R crystal structures. (A) Overall structure of inactive AT1R in complex with antagonist ZD7155 (green) and b562RIL (yellow). (B) Overall structure of active AT1R in complex with partial agonist S118 (magenta) and G-protein mimetic nanobody (cyan). (C) Major conformational changes between aligned inactive (blue) and active (orange) AT1R. Red arrows show obvious transmembrane (TM) movements during activation. The zoom-in views represent the distance between the C α atoms of L^{5.55} and N^{7.46} and the angle among the C α atoms of F^{6.34}, S^{6.47}, and V^{2.41}, in order to monitor the conformational rearrangements of TMs5-7. The superscripts refer to the Ballesteros-Weinstein numbering system.

Figure 2. (A) Conformational landscape of AT1R generated using the C α atom distance between L^{5.55} and N^{7.46}, and the angle among the C α atoms of F^{6.34}, S^{6.47}, and V^{2.41} as the order parameters along the activation pathway. (B) Projection of all reported active (red), inactive (blue), and intermediate (green) structures of class A GPCRs onto the AT1R conformational landscape. The unit of free-energy values is kcal/mol.

Figure 3: The three macrostates divided by Markov state model (MSM). (A) The distribution of three macrostates on the free energy landscape. The attribution and probability of each macrostate is shown on the right. (B) The transition time among the active, inactive, and intermediate states, represented by the mean first passage time (MFPT).

Figure 4: The comparison of representative inactive (A), intermediate (B), and active (C) structures. Zoom-in views of key structures are depicted on the right of (A), (B), and (C). Top left: the breaking of hydrophobic lock during activation. Top right: the activation renders the formation of a hydrogen bond between Y^{7.53} and Y^{5.58}. Bottom left: polar interaction on the position of common ionic lock is broken on the process of activation. Bottom right: F^{6.44} and F^{6.45} ratchet past F^{5.51} with the outward movement of TM6. Dynamic variations of these activation properties during a representative simulation

trajectory are shown in (D) for the distance between the C δ atom of R^{3.50} and the C γ atom of L^{6.30}, (E) for the area of the triangle composed of the C γ atom of L^{3.43}, the C β atom of V^{6.41}, and the C β atom of I^{6.40}, and (F) for the angle among the centroids of the benzene ring of F^{5.51}, F^{6.44}, and F^{6.45}.

Figure 5. The eight macrostates clustered by tICA. (A) The projection of eight macrostates on the landscape based on their C α distance between L^{5.55} and N^{7.46}, and the angle among the C α atoms of F^{6.34}, S^{6.47}, and V^{2.41}. (B) The transition time between the major six structures whose proportions are the most, presented in the form of the activation pathway.

Figure 6. The zoom-in view of the downstream partner binding area of backbone alignments of the two active conformers with GPCR–Gq and GPCR– β -arrestin structures. Macrostate 6 is depicted by orange cartoon and macrostate 7 is shown as purple cartoon. Gq and β -arrestin are colored in dark and light green, respectively. The clash between R^{3.50} and β -arrestin in the alternative conformation is shown in a red circle.

Figure 7. (A) All the pockets predicted by Fpocket in the intermediate state. Red circles show the overlap pockets with the prediction of inactive and active representative structures, while blue circles mean the intermediate-only pockets P6 and P9. (B) The alignment of current allosteric modulators on their sites with intermediate structure and pockets P2, P4, and P8. (C) The overlap of P9 with current allosteric GPCR modulators in crystal structures. In (B) and (C), cyan cartoons depict the intermediate AT1R and yellow sticks show corresponding pockets defined by Fpocket. Sticks in other colors show the allosteric modulators.

Figure 8. The emergence of P6 in other reported intermediate GPCR structures, where (A), (B), and (C) are B endothelin receptor (ETBR; PDB ID: 6IGK),⁶³ 5-hydroxytryptamine 1B subtype (5-HT_{1B}) receptor (PDB ID: 5V54),⁶⁴ and neurotensin receptor (NTSR1; PDB ID: 4XES).⁶⁵ The pocket closest to P6 are present in purple/blue/green sticks in (A), (B), (C), respectively. Other GPCRs are shown in gray cartoons. Pockets are detected by Fpocket in the same way of AT1R.

Figure 9. (A) The site of alanine scanning clusters on the 7TMs of AT1R, accomplished by gpcrdb database. AngII-induced Gq activation (B) and β -arrestin-2 recruitment (C) through wild-type (WT) AT1R and five cluster mutants. HEK293 cells transfected with each AT1R cluster mutant were compared with those transfected with the WT AT1R, n.s., no significant difference.

Figures

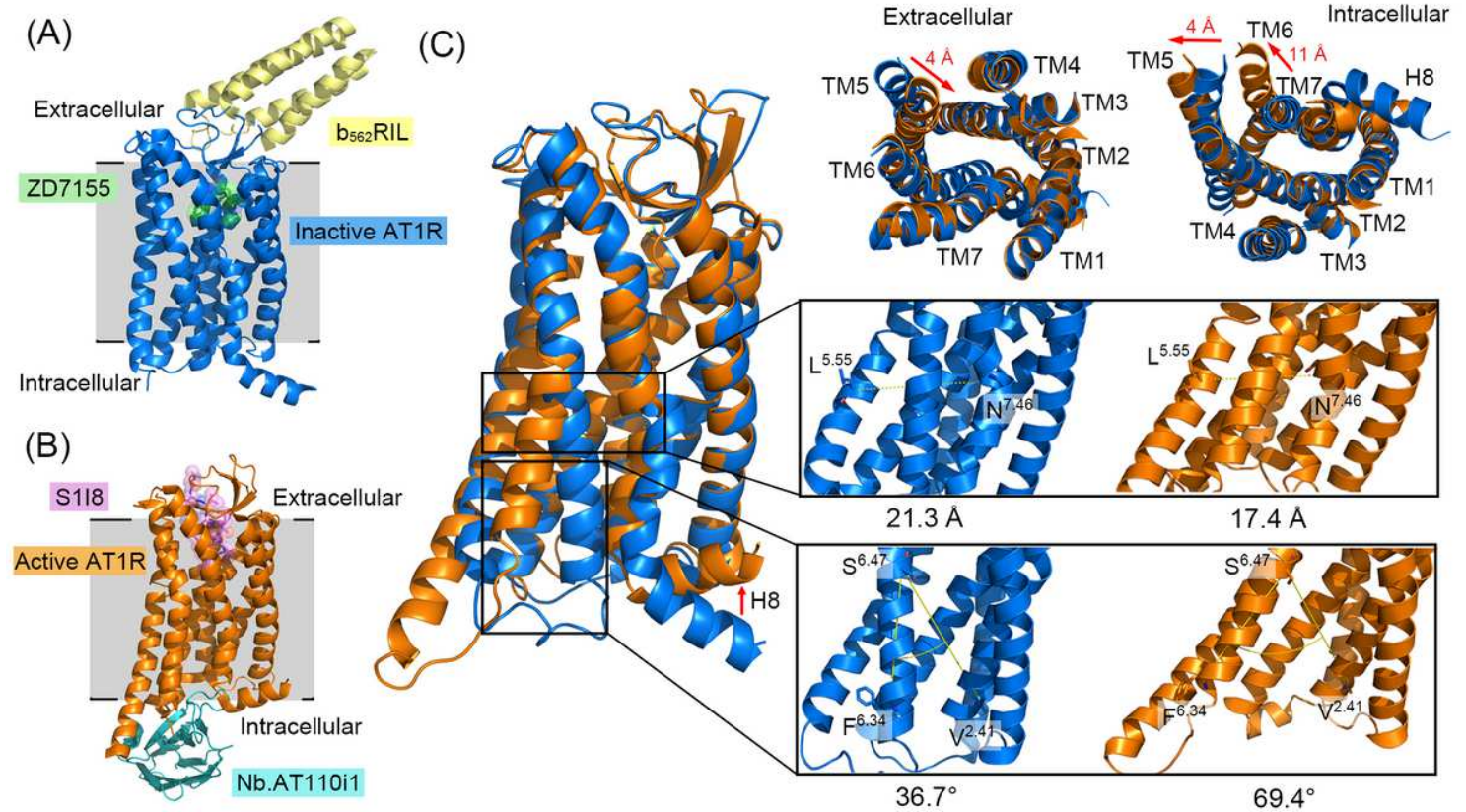


Figure 1

The distinction between inactive (PDB ID: 4YAY) and active (PDB ID: 6D01) AT1R crystal structures. (A) Overall structure of inactive AT1R in complex with antagonist ZD7155 (green) and b562RIL (yellow). (B) Overall structure of active AT1R in complex with partial agonist S118 (magenta) and G-protein mimetic nanobody (cyan). (C) Major conformational changes between aligned inactive (blue) and active (orange) AT1R. Red arrows show obvious transmembrane (TM) movements during activation. The zoom-in views represent the distance between the Ca atoms of L^{5.55} and N^{7.46} and the angle among the Ca atoms of F^{6.34}, S^{6.47}, and V^{2.41}, in order to monitor the conformational rearrangements of TMs5-7. The superscripts refer to the Ballesteros-Weinstein numbering system.

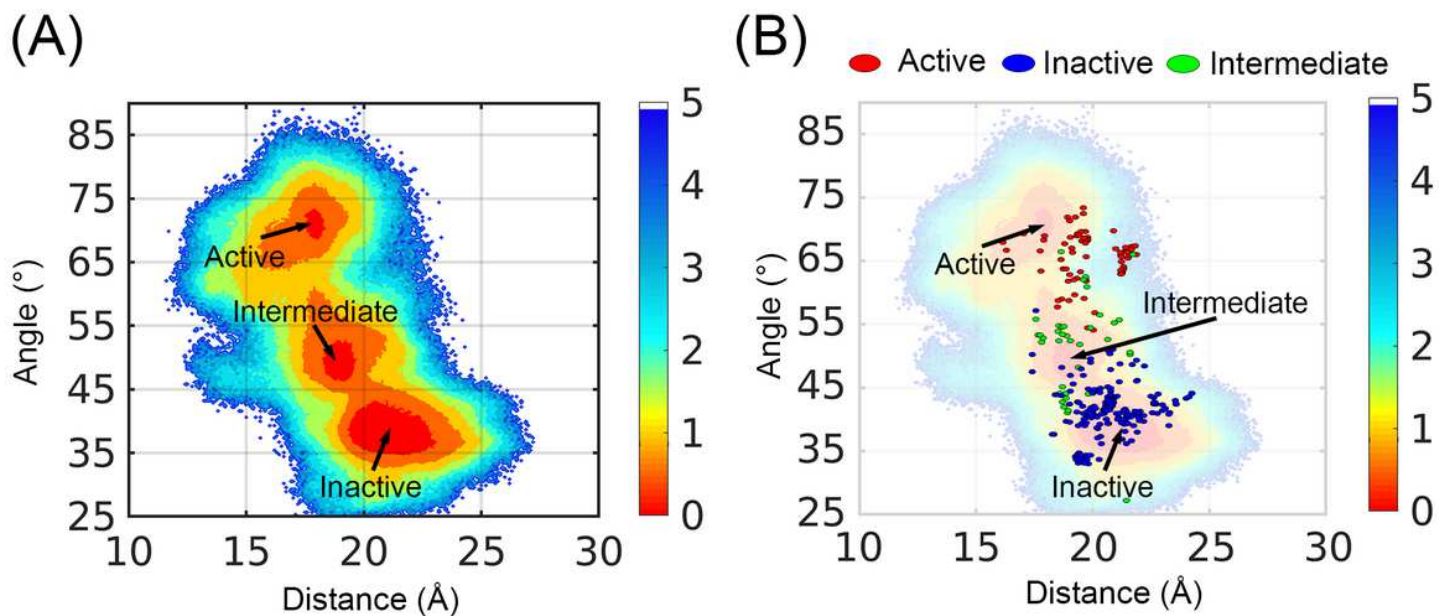


Figure 2

(A) Conformational landscape of AT1R generated using the C α atom distance between L5.55 and N7.46, and the angle among the C α atoms of F6.34, S6.47, and V2.41 as the order parameters along the activation pathway. (B) Projection of all reported active (red), inactive (blue), and intermediate (green) structures of class A GPCRs onto the AT1R conformational landscape. The unit of free-energy values is kcal/mol.

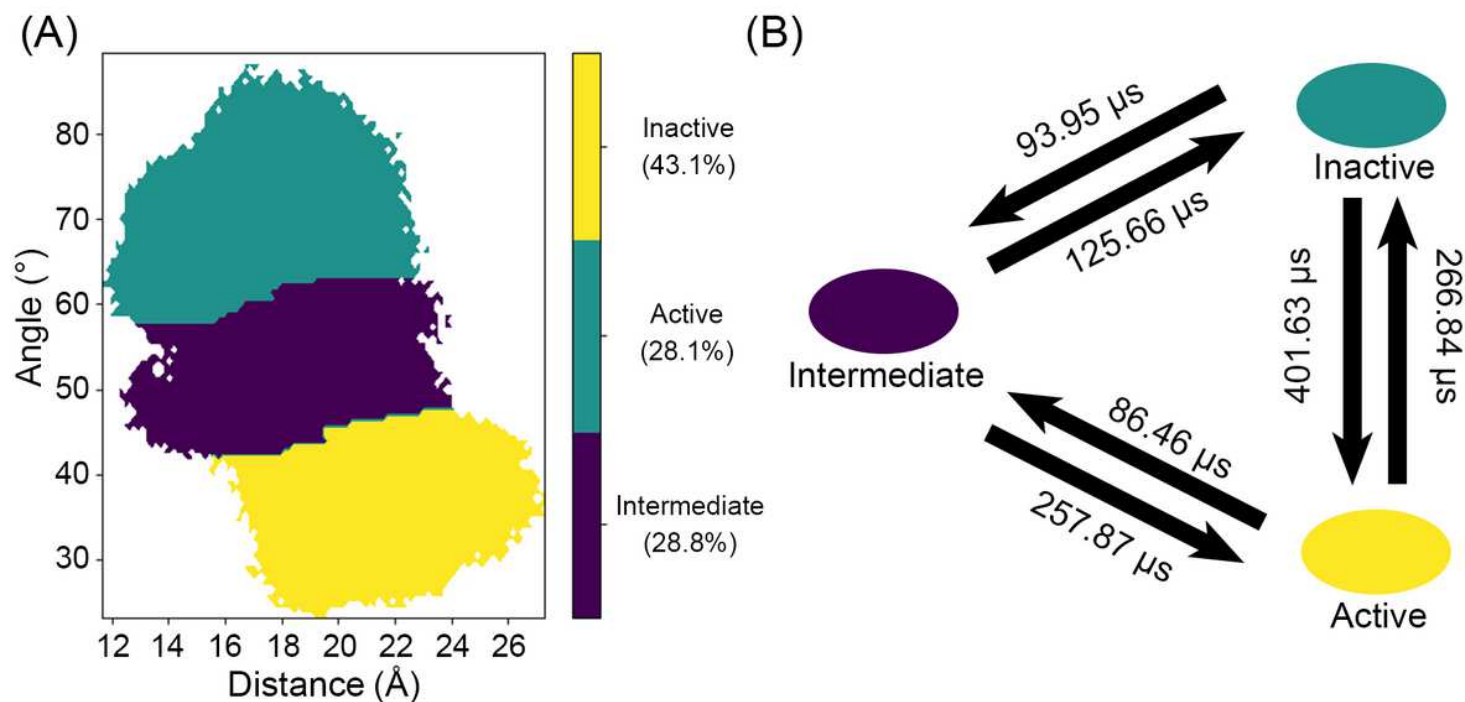


Figure 3

The three macrostates divided by Markov state model (MSM). (A) The distribution of three macrostates on the free energy landscape. The attribution and probability of each macrostate is shown on the right. (B) The transition time among the active, inactive, and intermediate states, represented by the mean first passage time (MFPT).

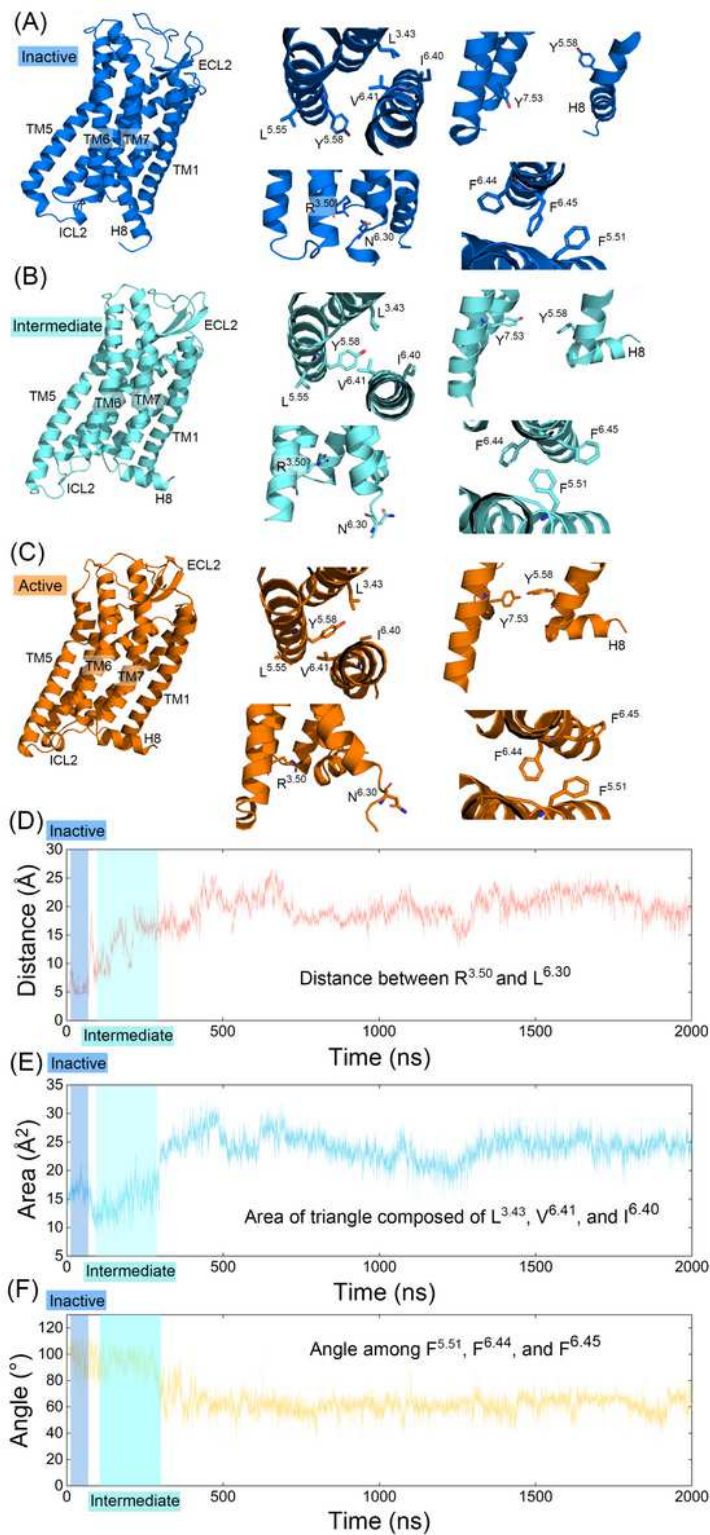


Figure 4

The comparison of representative inactive (A), intermediate (B), and active (C) structures. Zoom-in views of key structures are depicted on the right of (A), (B), and (C). Top left: the breaking of hydrophobic lock during activation. Top right: the activation renders the formation of a hydrogen bond between Y7.53 and Y5.58. Bottom left: polar interaction on the position of common ionic lock is broken on the process of activation. Bottom right: F6.44 and F6.45 ratchet past F5.51 with the outward movement of TM6. Dynamic variations of these activation properties during a representative simulation trajectory are shown in (D) for the distance between the C α atom of R3.50 and the C γ atom of L6.30, (E) for the area of the triangle composed of the C γ atom of L3.43, the C β atom of V6.41, and the C β atom of I6.40, and (F) for the angle among the centroids of the benzene ring of F5.51, F6.44, and F6.45.

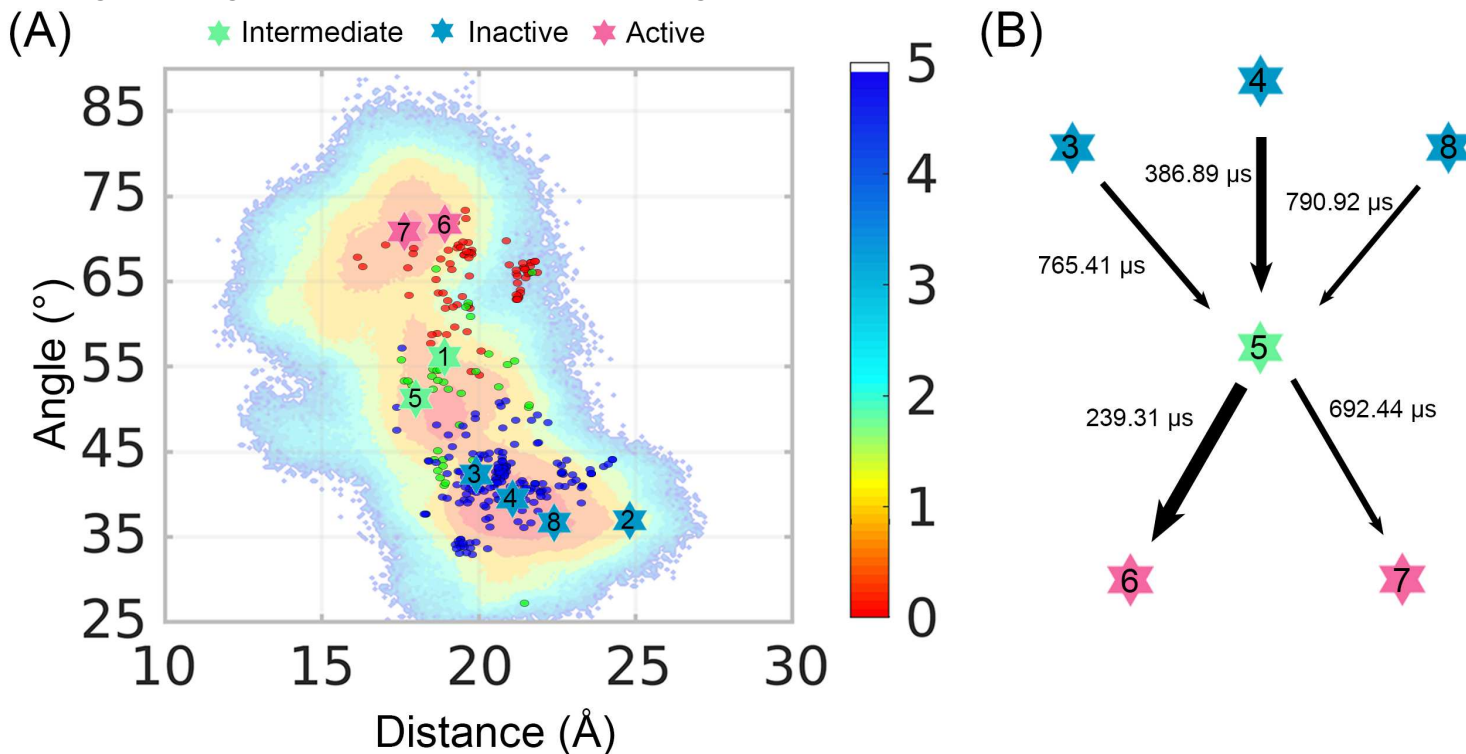
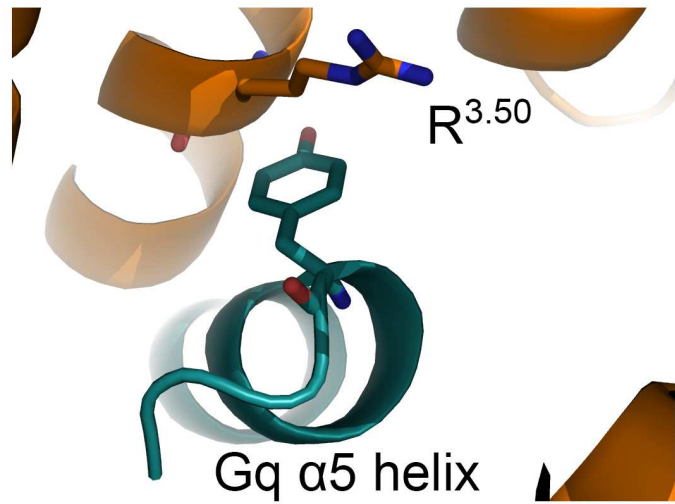


Figure 5

The eight macrostates clustered by tICA. (A) The projection of eight macrostates on the landscape based on their Calpha distance between L5.55 and N7.46, and the angle among the Calpha atoms of F6.34, S6.47, and V2.41. (B) The transition time between the major six structures whose proportions are the most, presented in the form of the activation pathway.

6-canonical active conformation



7-alternative active conformation

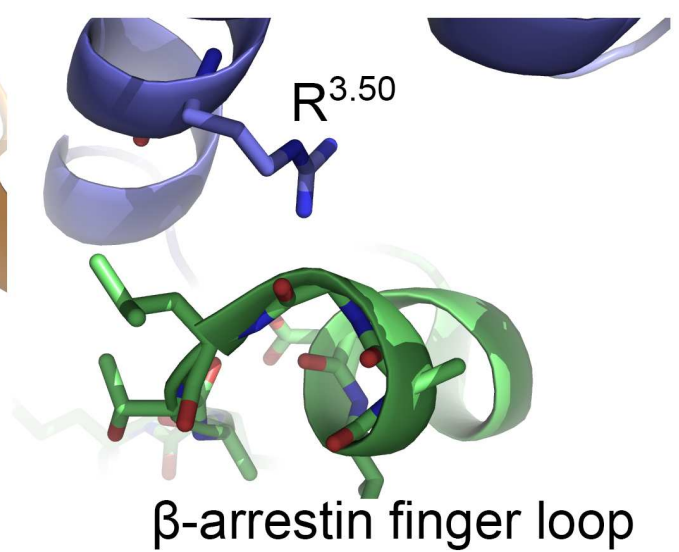
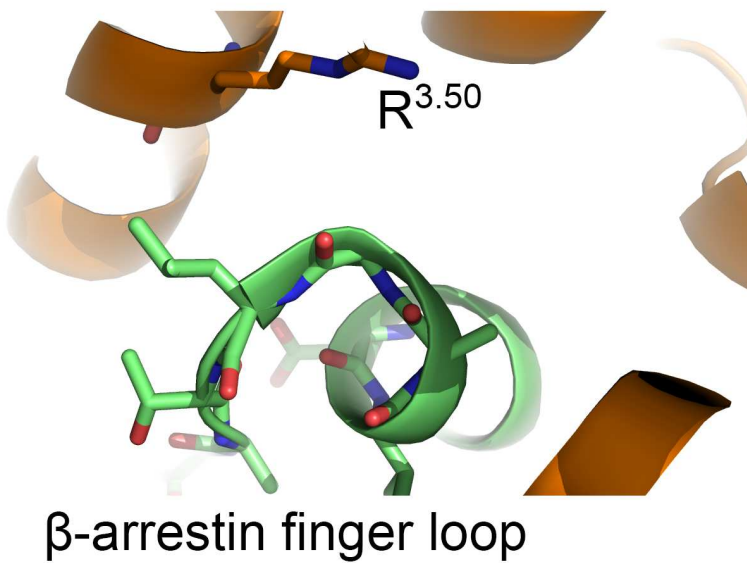
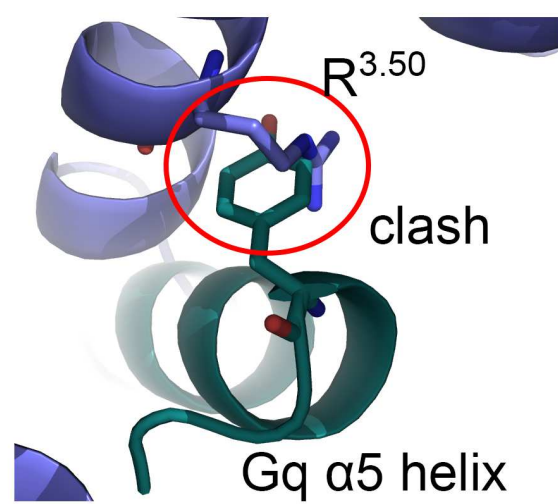


Figure 6

The zoom-in view of the downstream partner binding area of backbone alignments of the two active conformers with GPCR-Gq and GPCR- β -arrestin structures. Macrostate 6 is depicted by orange cartoon and macrostate 7 is shown as purple cartoon. Gq and β -arrestin are colored in dark and light green, respectively. The clash between R^{3.50} and β -arrestin in the alternative conformation is shown in a red circle.

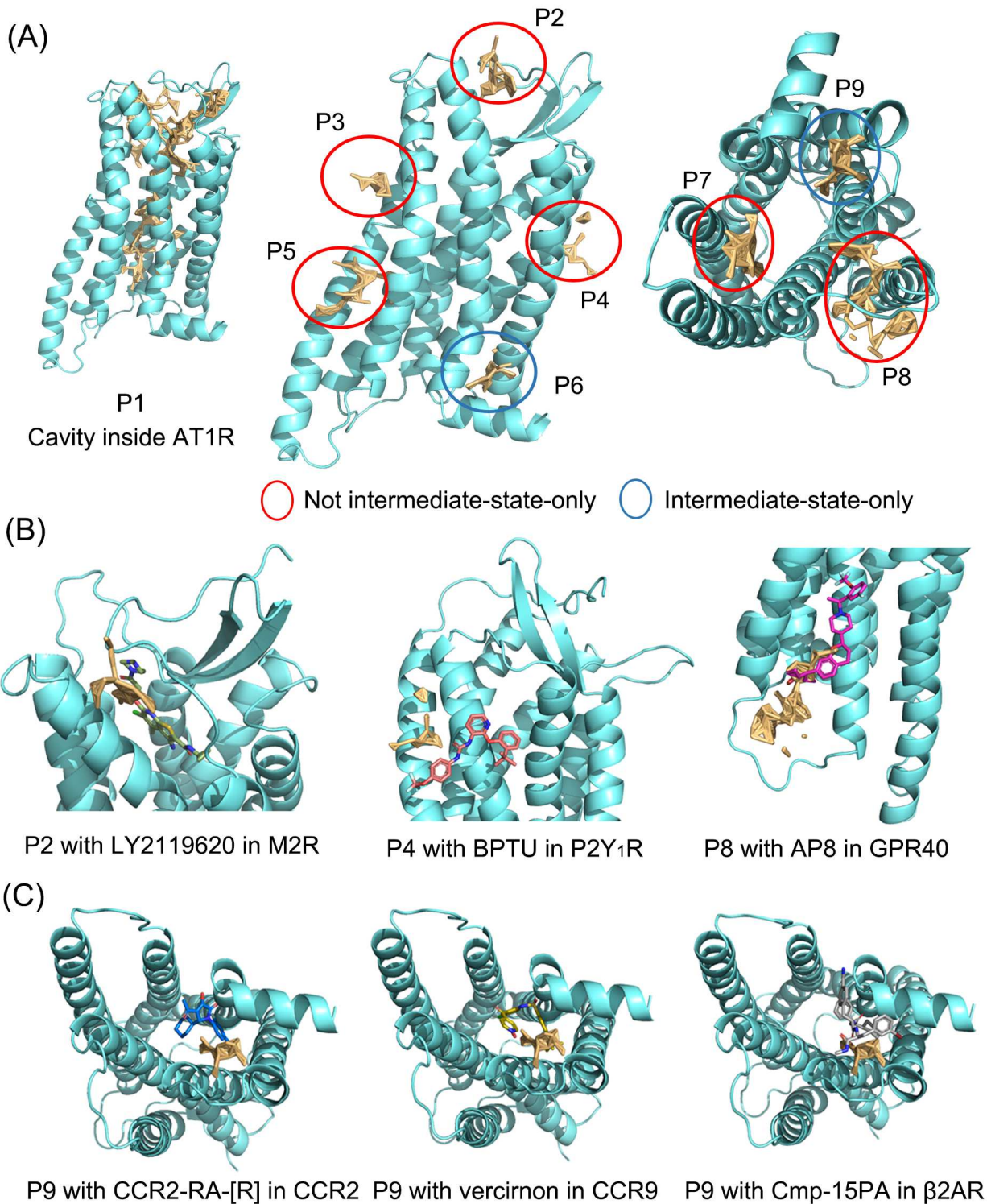


Figure 7

(A) All the pockets predicted by Fpocket in the intermediate state. Red circles show the overlap pockets with the prediction of inactive and active representative structures, while blue circles mean the intermediate-only pockets P6 and P9. (B) The alignment of current allosteric modulators on their sites with intermediate structure and pockets P2, P4, and P8. (C) The overlap of P9 with current allosteric GPCR modulators in crystal structures. In (B) and (C), cyan cartoons depict the intermediate AT1R and yellow

sticks show corresponding pockets defined by Fpocket. Sticks in other colors show the allosteric modulators.

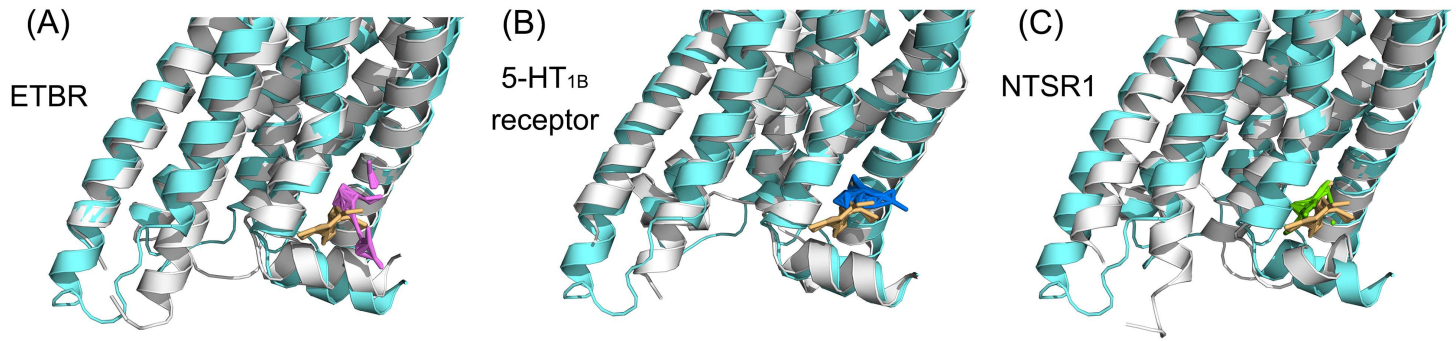


Figure 8

The emergence of P6 in other reported intermediate GPCR structures, where (A), (B), and (C) are B endothelin receptor (ETBR; PDB ID: 6IGK),⁶³ 5-hydroxytryptamine 1B subtype (5-HT_{1B}) receptor (PDB ID: 5V54),⁶⁴ and neurotensin receptor (NTSR1; PDB ID: 4XES).⁶⁵ The pocket closest to P6 are present in purple/blue/green sticks in (A), (B), (C), respectively. Other GPCRs are shown in gray cartoons. Pockets are detected by Fpocket in the same way of AT1R.

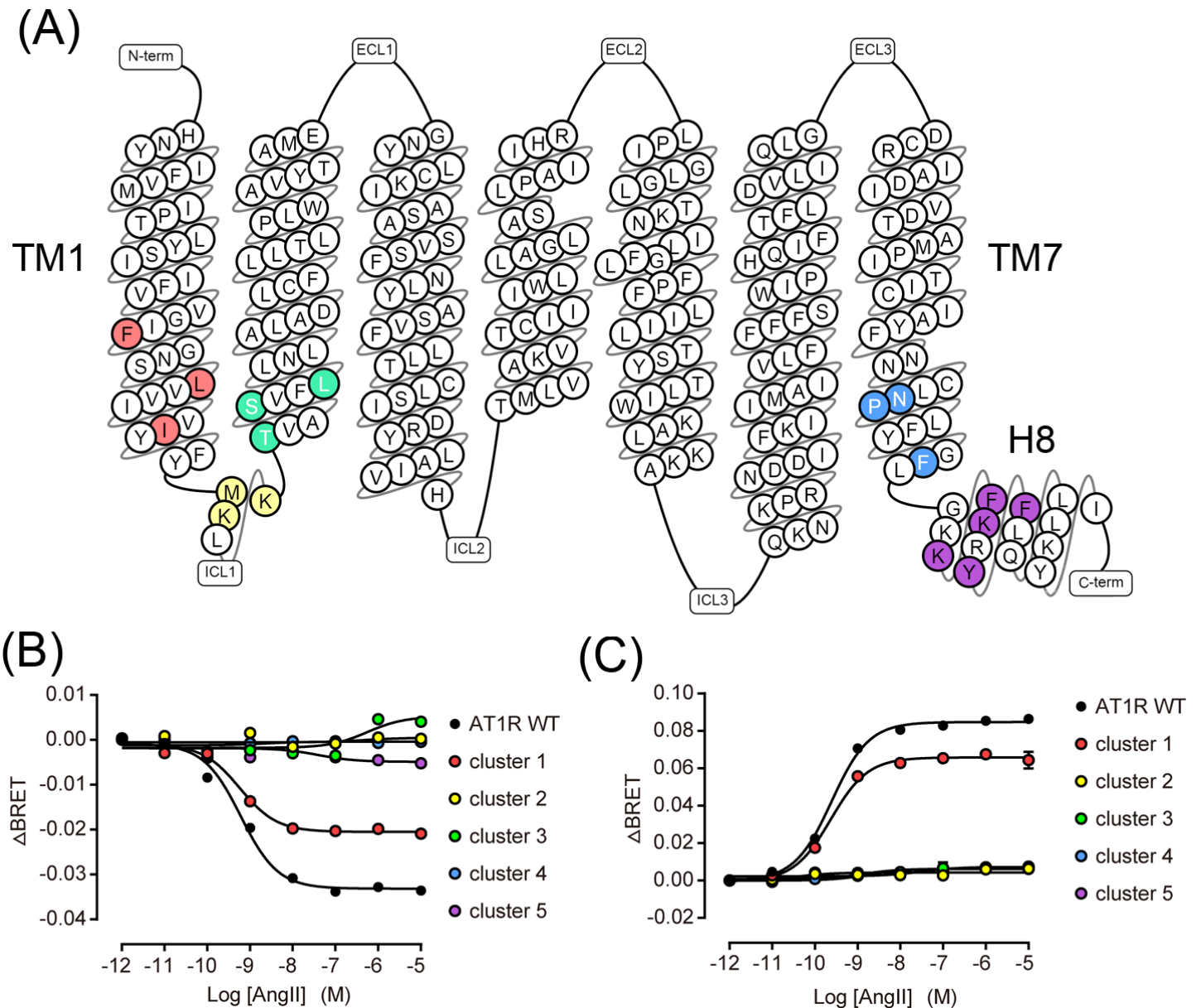


Figure 9

(A) The site of alanine scanning clusters on the 7TMs of AT1R, accomplished by gpcrdB database. AngII-induced Gq activation (B) and β -arrestin-2 recruitment (C) through wild-type (WT) AT1R and five cluster mutants. HEK293 cells transfected with each AT1R cluster mutant were compared with those transfected with the WT AT1R, n.s., no significant difference.

Supplementary Files

This is a list of supplementary files associated with this preprint. Click to download.

- [SupportingInformation.docx](#)